

Space-time wave packets localized in all dimensions

Received: 4 November 2021

Accepted: 20 July 2022

Published online: 05 August 2022

 Check for updates

Murat Yessenov¹✉, Justin Free², Zhaozhong Chen³, Eric G. Johnson²,
Martin P. J. Lavery³, Miguel A. Alonso^{4,5} & Ayman F. Abouraddy¹✉

Optical wave packets that are localized in space and time, but nevertheless overcome diffraction and travel rigidly in free space, are a long sought-after field structure with applications ranging from microscopy and remote sensing, to nonlinear and quantum optics. However, synthesizing such wave packets requires introducing non-differentiable angular dispersion with high spectral precision in two transverse dimensions, a capability that has eluded optics to date. Here, we describe an experimental strategy capable of sculpting the spatio-temporal spectrum of a generic pulsed beam by introducing arbitrary radial chirp via two-dimensional conformal coordinate transformations of the spectrally resolved field. This procedure yields propagation-invariant ‘space-time’ wave packets localized in all dimensions, with tunable group velocity in the range from $0.7c$ to $1.8c$ in free space, and endowed with prescribed orbital angular momentum. By providing unprecedented flexibility in sculpting the three-dimensional structure of pulsed optical fields, our experimental strategy promises to be a versatile platform for the emerging enterprise of space-time optics.

Creating spatio-temporally localized optical wave packets that overcome diffraction and propagate rigidly in free space has been a long-standing yet elusive goal in optics. Such wave packets can have applications ranging from remote optical sensing and biological imaging, to nonlinear and quantum optics. To date, this challenge has been addressed via nonlinear optical effects that sustain solitons¹, waveguiding structures², or by exploiting particularly shaped waveforms such as Bessel-Airy wave packets in linear dispersive media³. Propagation invariance in a linear nondispersive medium necessitates inculcating a precise spatio-temporal spectral structure into the field by introducing angular dispersion (AD)^{4,5}; i.e., associating each wavelength with a single propagation direction^{6,7}. Examples of such wave packets date back to Brittingham’s focus-wave mode⁸, X-waves^{9,10}, and more recently the general class of ‘space-time’ (ST) wave packets^{11–19}. The challenge of producing the AD necessary for propagation-invariant wave packets localized in all dimensions (referred to hereon as 3D ST

wave packets) is twofold. First, the AD must be inculcated in two transverse dimensions rather than in one as typically realized via gratings or prisms^{4,5}. Second, non-differentiable AD is required²⁰; i.e., it is necessary that the derivative of the wavelength-dependent propagation angle not be defined at some wavelength^{21,22} – a field configuration that cannot be directly produced with conventional optical components. Consequently, with the exception of X-waves that are AD-free, no propagation-invariant optical wave packets that are localized in all dimensions have been observed in free space⁷.

The challenge of introducing arbitrary AD into a generic pulsed beam along one transverse dimension has been recently addressed by constructing a universal AD synthesizer²³. This experimental strategy has enabled the realization of ST wave packets in the form of light sheets¹⁶ (referred to hereon as 2D ST wave packets), which exhibit a broad host of sought-after effects, such as long-distance propagation invariance²⁴, tunable group velocities^{13,25–29}, anomalous refraction at

¹CREOL, The College of Optics & Photonics, University of Central Florida, Orlando, FL 32816, USA. ²Micro-Photonics Laboratory, the Holcombe Department of Electrical and Computer Engineering, Clemson University, Clemson, SC 29634, USA. ³James Watt School of Engineering, University of Glasgow, Glasgow, UK. ⁴CNRS, Centrale Marseille, Institut Fresnel, Aix Marseille Univ., Marseille, France. ⁵The Institute of Optics, University of Rochester, Rochester, NY, USA.

✉ e-mail: yessenov@knights.ucf.edu; raddy@creol.ucf.edu

planar interfaces³⁰, and the space-time Talbot effect³¹. Although this arrangement produces non-differentiable AD with high spectral resolution, these features cannot be extended to both transverse dimensions. Crucially, the centerpiece of this configuration is a spatial light modulator that modifies the temporal spectrum along one dimension, leaving only one dimension to manipulate the field spatially – a limitation that is shared by other recently investigated spatio-temporal field structures^{32–39}. Therefore, the fundamental challenge of producing non-differentiable AD encompassing both transverse dimensions remains outstanding.

Here, we demonstrate a spatio-temporal modulation strategy that efficiently produces arbitrary yet precise AD in two transverse dimensions, and thus yields ST wave packets localized in all dimensions – while preserving all the key attributes of its reduced-dimension counterpart. This modulation scheme is implemented in three stages. In the first stage, the spectrum of a generic plane-wave pulse is spatially resolved along one dimension after a double-pass through a volume chirped Bragg grating. In the second stage, a spectral transformation ‘reshuffles’ the wavelengths into a prescribed sequence. In the third stage, a log-polar-to-Cartesian conformal coordinate transformation converts the spatial locus of each wavelength from a line into a circle^{40,41}. A lens finally converts the spectrally resolved wave front into a 3D ST wave packet localized in all three dimensions. Utilizing this approach, we produce 3D ST wave packets with $\approx 30 \mu\text{m}$ transverse beam width and $\approx 6 \text{ ps}$ pulse width that propagate for over 50 mm. Moreover, by modulating the spatio-temporal spectral structure, we realize group velocities extending from the subluminal to the superluminal regimes over the range from $0.7c$ to $1.8c$ (c is the speed of light in vacuum). Furthermore, by providing access to both transverse dimensions in a ST wave packet, new degrees of freedom of the optical field can be accessed, such as orbital angular momentum (OAM)^{42–44}. Specifically, by encoding a helical phase structure in the spatio-temporal spectrum, we demonstrate propagation-invariant pulsed OAM wave packets with controllable group velocity in free space, which we refer to as ST-OAM wave packets. In addition to the propagation-invariance and arbitrary group velocities of ST-OAM wave packets, their underlying spatio-temporal structure may lead to variations of some of the recently uncovered behaviors of conventional OAM pulses, such as the trade-off between the topological charge and pulse duration^{43,45,46}. Such 3D ST wave packets that are fully localized in all dimensions have potential uses in areas such as free-space optical communications, imaging, and nonlinear optics.

Results

Theory of 3D space-time wave packets

A useful conceptual tool for understanding the characteristics of ST wave packets and the requirements for their synthesis is to visualize their spectral support domain on the surface of the light cone. The light-cone is the geometric representation of the free-space dispersion relationship $k_x^2 + k_y^2 + k_z^2 = (\frac{\omega}{c})^2$, where ω is the temporal frequency, c is the speed of light in vacuum, (k_x, k_y, k_z) are the components of the wave vector in the Cartesian coordinate system (x, y, z) , x and y are the transverse coordinate, and z is the axial coordinate. Although this relationship corresponds to the surface of a four-dimensional hyper-cone, a useful representation follows from initially restricting our attention to azimuthally symmetric fields in which k_x and k_y are combined into a radial wave number $k_r = \sqrt{k_x^2 + k_y^2}$, so that the light-cone can be then visualized in $(k_r, k_z, \frac{\omega}{c})$ -space (Fig. 1). The spectral support domain for 3D ST wave packets is restricted to the conic section at the intersection of the light-cone with a spectral plane that is parallel to the k_r -axis and makes an angle θ (the spectral tilt angle) with the k_z -axis, which is given by the equation $\Omega = (k_z - k_0)c \tan \theta$; here $\Omega = \omega - \omega_0$, ω_0 is a carrier frequency, and $k_0 = \omega_0/c$. It can be readily shown that such a

construction in the narrowband paraxial regime results in a propagation-invariant 3D ST wave packet $E(r, z; t) = e^{i(k_0 z - \omega_0 t)} \psi(r, z; t)$, where the slowly varying envelope $\psi(r, z; t)$ travels rigidly at a group velocity $\tilde{v} = c \tan \theta$, $\psi(r, z; t) = \psi(r, 0; t - z/\tilde{v})$, where $\psi(r, 0; t) = \int dk_r k_r \tilde{\psi}(k_r) \mathcal{J}_0(k_r r) e^{-i\Omega t}$, and $\tilde{\psi}(k_r)$ is the spectrum. Here k_r and Ω are no longer independent variables, but are instead related via the particular spectral trajectory on the light-cone (Supplementary Note 1). Although this spectral trajectory is a conic section whose kind is determined by the spectral tilt angle θ , it can nevertheless be approximated in the narrowband paraxial regime by a parabola in the vicinity of $k_r = 0$:

$$\frac{\Omega}{\omega_0} = \frac{k_r^2}{2k_0^2(1 - \tilde{n})}, \tag{1}$$

where $\tilde{n} = \cot \theta$ is the wave-packet group index in free space. By setting $k_r = k \sin \varphi(\omega)$, where $\varphi(\omega)$ is the propagation angle for ω as shown in Fig. 1a, we have $\varphi(\omega) \approx \eta \sqrt{\frac{\Omega}{\omega_0}}$, which is not differentiable at $\Omega = 0$ ^{20,23}; here $\tilde{n} = 1 - \frac{\sigma}{2} \eta^2$, $\sigma = 1$ in the superluminal regime, and $\sigma = -1$ in the subluminal regime. In other words, non-differentiable AD is required to produce a propagation-invariant ST wave packet. This result is similar to that for ST light-sheets¹⁶ except that the transverse coordinate x is now replaced with the radial coordinate r .

The representation in Fig. 1 is particularly useful in identifying a path towards synthesizing 3D ST wave packets. When $45^\circ < \theta < 90^\circ$, the ST wave packet is superluminal $\tilde{v} > c$, Ω is positive, and ω_0 is the minimum allowable frequency in the spectrum. When viewed in $(k_x, k_y, \frac{\omega}{c})$ -space, the wavelengths are arranged in concentric circles, with long wavelengths (low frequencies) at the center, and shorter wavelengths (higher frequencies) extending outward. On the other hand, when $0^\circ < \theta < 45^\circ$, the ST wave packet is subluminal $\tilde{v} < c$, Ω is negative, and ω_0 is the maximum allowable frequency in the spectrum. The wavelengths are again arranged in concentric circles in $(k_x, k_y, \frac{\omega}{c})$ -space – but in the opposite order: short wavelengths are close to the center and longer wavelengths extend outward. For both subluminal and superluminal 3D ST wave packets, each ω is associated with a single radial spatial frequency $k_r(\omega)$, and is related to it via the relationship in Eq. (1). This representation indicates the need for arranging the wavelengths in concentric circles with square-root radial chirp, and then converting the spatial spectrum into physical space via a spherical lens. Moreover, adding a spectral phase factor $e^{i\ell\chi}$, where ℓ is an integer and χ is the azimuthal angle in spectral space, produces OAM in physical space (Supplementary Note 1B).

Closed-form expressions can be obtained for 3D ST wave packets by applying Lorentz boosts to an appropriate initial field^{47–50}. For example, starting with a monochromatic beam $E_0(r, z; t)$, a subluminal 3D ST wave packet at a group velocity \tilde{v} is obtained by the Lorentz boost $E(r, z; t) = E_0(r, \frac{z - \tilde{v}t}{\sqrt{1 - \beta^2}}; \frac{t - \tilde{v}z/c^2}{\sqrt{1 - \beta^2}})$, where $\beta = \frac{\tilde{v}}{c}$ is the Lorentz factor.

On the other hand, closed-form expressions for superluminal 3D ST wave packets can be obtained by applying a Lorentz boost to the ‘needle beam’ in¹². The time-averaged intensity is $I(r, \varphi, z) = 2\pi k_0^2(1 - \tilde{n}) \int dk_r k_r^2 |\tilde{\psi}(k_r)|^2 J_0^2(k_r r)$, which is independent of φ even if the field is endowed with OAM. In the case of 2D ST light-sheets, the time-averaged intensity separates into a sum of a constant background pedestal and a spatially localized feature at the center¹⁶. A similar decomposition is not possible for 3D ST wave packets. However, using the asymptotic form for Bessel functions that is valid far from $r = 0$, we have:

$$I(r) \approx \frac{2\pi k_0^2(1 - \tilde{n})}{\pi r} \int dk_r \sqrt{k_0^2 + k_r^2} |\tilde{\psi}(k_r)|^2 + \frac{2\pi k_0^2(1 - \tilde{n})(-1)^\ell}{\pi r} \int dk_r \sqrt{k_0^2 + k_r^2} |\tilde{\psi}(k_r)|^2 \sin(2k_r r), \tag{2}$$

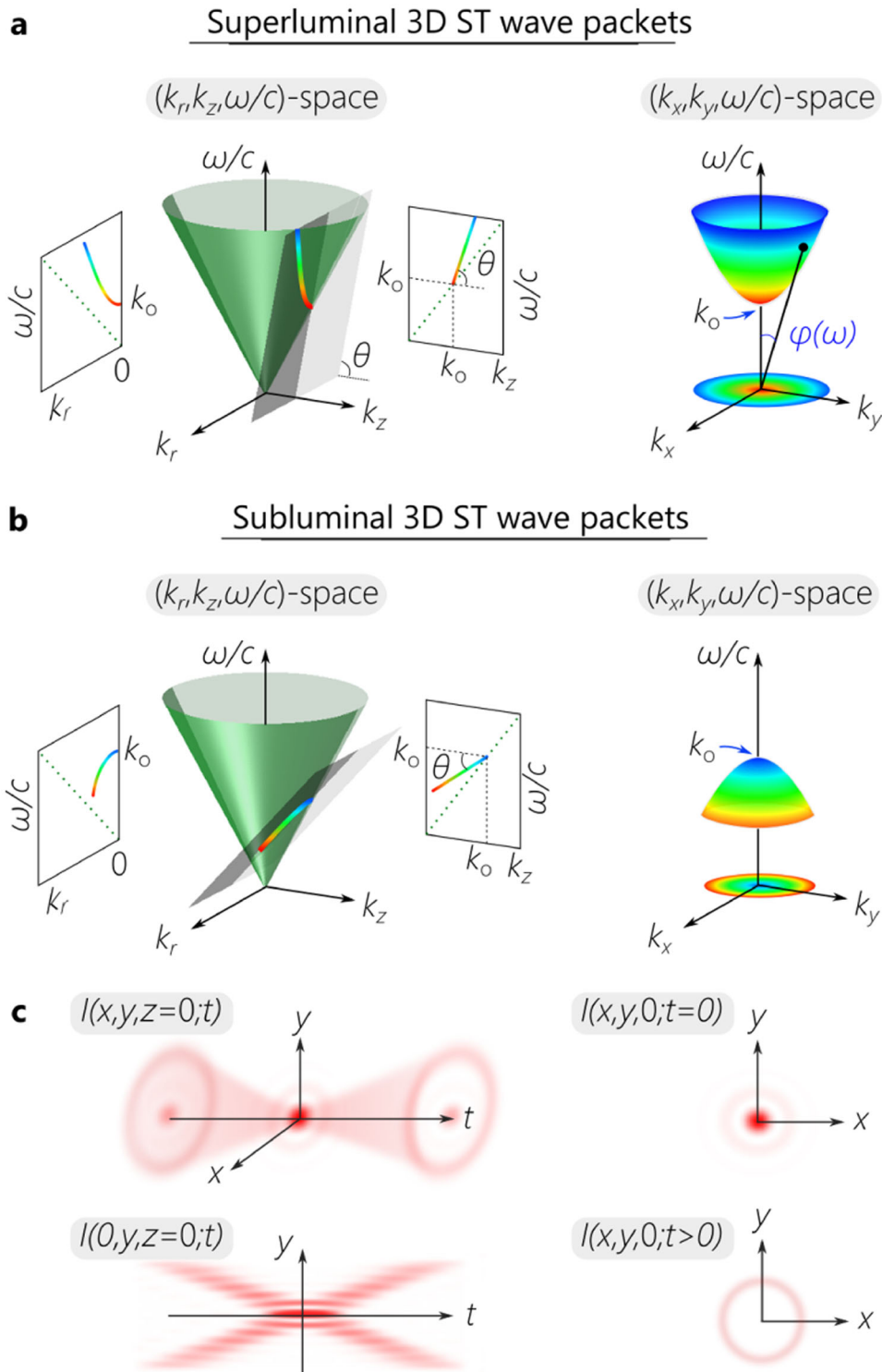


Fig. 1 | Visualization of the spectral support domain for 3D ST wave packets on the surface of the free-space light-cone. **a** The spectral support domain for a superluminal 3D ST wave packet at the intersection of the light-cone $k_r^2 + k_z^2 = (\frac{\omega}{c})^2$ with a spectral plane that is parallel to the k_r -axis and makes an angle $\theta > 45^\circ$ with the k_z -axis. The conic section at the intersection is a hyperbola. In $(k_x, k_y, \frac{\omega}{c})$ -space the spectrum is one half of a two-sheet hyperboloid (an elliptic hyperboloid). **b** Same as

a for a subluminal ST wave packet with $\theta < 45^\circ$, where the spectral support domain on the light-cone in $(k_r, k_z, \frac{\omega}{c})$ -space is an ellipse. In $(k_x, k_y, \frac{\omega}{c})$ -space, the spectrum is an ellipsoid of revolution (a spheroid, which may be prolate or oblate according to the value of θ). **c** Plot of the spatio-temporal intensity profile $I(x, y, z=0; t)$ at a fixed axial plane $z=0$, the intensity profile in a meridional plane $I(0, y, z=0; t)$, and the transverse profiles at the wave-packet center $I(x, y, 0; 0)$ and off-center $I(x, y, 0; t > 0)$.

where the first term is a pedestal decaying at a rate of $\frac{1}{r}$, and the second term tends to be localized closer to the beam center. In the vicinity of $r=0$, the two terms merge and cannot be separated. The spatio-temporal intensity profile of such a 3D ST wave packet is depicted in

Fig. 1c: two conic field structures emanate from the wave-packet center, such that the profile is X-shaped in any (meridional plane containing the optical axis, and the intensity profile is circularly symmetric in any transverse plane.

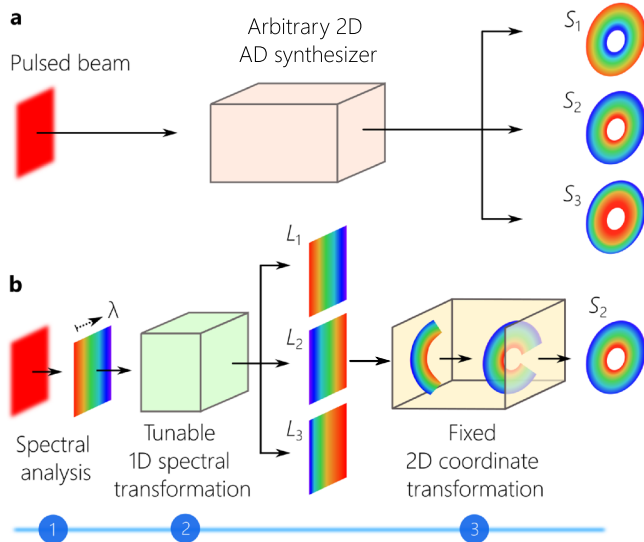


Fig. 2 | Synthesis strategy for 3D ST wave packets. **a** Starting with a generic plane-wave pulse, we aim at constructing an angular-dispersion synthesizer in two dimensions that arranges the wavelengths in circles in a prescribed order. S_1 corresponds to a subluminal wave packet, whereas S_2 and S_3 correspond to superluminal wave packets of different group velocities. **b** The proposed strategy comprises spectral analysis followed by a tunable 1D spectral transformation that rearranges the initial wavelength sequence in the spectrally resolved wavefront. The 1D spectra L_1 , L_2 , and L_3 are rectilinear counterparts of S_1 , S_2 , and S_3 in **a**. In the third stage, a fixed 2D conformal coordinate transformation converts vertical lines into circles, thereby realizing the targeted spatio-temporal spectra S_1 , S_2 , and S_3 .

Synthesizing ST wave packets localized in all dimensions

Central to converting a generic pulsed beam into a ST wave packet localized in all dimensions is the construction of an optical scheme that can associate each wavelength λ with a particular azimuthally symmetric spatial frequency $k_r(\lambda)$ and arrange the wavelengths in concentric circles with the order prescribed in Eq. (1) (Fig. 2a). This system realizes two functionalities, producing a particular wavelength sequence, and changing the coordinate system, which are implemented in succession via the three-stage strategy outlined in Fig. 2b. In the first stage, the spectrum of a plane-wave pulse is resolved along one spatial dimension. At this point, the field is endowed with linear spatial chirp and the wavelengths are arranged in a fixed sequence. The second stage rearranges the wavelengths in a new prescribed sequence. This spectral transformation is tunable; that is, a wide range of spectral structures can be obtained from a fixed input. In the third stage, a 2D conformal transformation converts the coordinate system to map the rectilinear chirp into a radial chirp; i.e., lines corresponding to different wavelengths at the input are converted into circles at the output^{40,41}. Because the spectral transformation in the second stage is tunable, the 2D coordinate transformation can be held fixed. In this way, we obtain arbitrary (including non-differentiable) AD in two dimensions.

The layout of the experimental setup is depicted in Fig. 3. We start off in the first stage with pulses from a Ti:sapphire laser (pulse width ≈ 100 fs and bandwidth ≈ 10 nm at a central wavelength of ≈ 800 nm). Because a flat-phase front is critical for successfully implementing the subsequent transformations, the use of conventional surface gratings is precluded, and we utilize instead a double-pass configuration through a volume chirped Bragg grating (CBG). The CBG resolves the spectrum horizontally along the x -axis and introduces linear spatial chirp so that $x_1(\lambda) = \alpha(\lambda - \lambda_0)$; where α is the linear spatial chirp rate⁵¹, λ_0 is a fixed wavelength, and the bandwidth utilized is $\Delta\lambda \approx 0.3$ nm. It is crucial that this task be achieved with high spectral resolution. Previous studies have shown that the critical parameter determining the propagation distance of ST wave packets is the ‘spectral uncertainty’

$\delta\lambda$, which is the finite spectral uncertainty in the association between spatial and temporal frequencies⁵². Our measurements indicate that the optimal spectral uncertainty after the CBG arrangement is $\delta\lambda \approx 35$ pm, which is achieved for a 2-mm input beam width (Supplementary Fig. 11).

The second stage of the synthesis strategy is a 1D spatial transformation along the x -axis to rearrange the wavelength sequence, thereby implementing a spectral transformation. Specifically, each wavelength λ is transposed from $x_1(\lambda)$ at the input via a logarithmic mapping to $x_2(\lambda) = A \ln(\frac{x_1(\lambda)}{B})$ at the output. This transformation is realized via two phase patterns implemented by a pair of spatial light modulators (SLMs) to enable tuning the transformation parameters A and B . This particular ‘reshuffling’ of the wavelength sequence pre-compensates the exponentiation included in the subsequent coordinate transformation. By tuning the value of B , we can vary the group velocity \tilde{v} over the subluminal and superluminal regimes (Supplementary Table 1).

In the third stage we perform a log-polar-to-Cartesian coordinate transformation: $(x_2, y_2) \rightarrow (r, \varphi)$ via the 2D mapping: $r(\lambda) = C \exp(-\frac{x_2(\lambda)}{D})$ and $\varphi = \frac{y_2}{D}$ ^{40,41}. The exponentiation here is pre-compensated by the logarithmic mapping in the 1D spectral transformation, and the wavelength at position $x_2(\lambda)$ at the input is converted into a circle of radius $r(\lambda) \propto (\lambda - \lambda_0)^{A/D}$ at the output. This 2D coordinate transformation was developed decades ago^{40,41}, and was recently revived as a methodology for sorting OAM modes^{53,54}. We operate the system in reverse (lines-to-circles, rather than the more typical circles-to-lines⁵³), and we make use of a polychromatic field (rather than monochromatic field). The exponent of the chirp rate depends only on the ratio $\frac{A}{D}$, so that setting $D = 2A$ yields $r(\lambda) \propto \sqrt{\lambda - \lambda_0}$ in accordance with Eq. (1). The wavelengths are arranged with square-root radial chirp, thereby realizing the required non-differentiable AD. Finally, a spherical converging lens of focal length f generates the 3D ST wave packets in physical space, equivalently mapping $r \rightarrow k_r = k \frac{r}{f}$.

The 2D coordinate transformation is performed with two different embodiments: using a pair of diamond-machined refractive phase plates⁵⁴, and using a pair of diffractive phase plates⁵⁵, which yielded similar performance. Because both of these realizations are stationary, the values of C and D are fixed. The data reported in Fig. 4 through Fig. 7 made use of the refractive phase plates with $C = 4.77$ mm and $D = 1$ mm. Moreover, fixing the value of D entails in turn fixing the value of A to maintain $A = D/2$. The group velocity $\tilde{v} = c/\tilde{n}$ is tuned over the subluminal and superluminal regimes by varying B , whereby $\tilde{n} \approx 1 - \frac{2.24}{B}$, with B in units of mm [Supplementary Note 2].

This experimental strategy provides two pathways for introducing OAM into the 3D ST wave packet. One may utilize a conventional spiral phase plate to imprint an OAM order ℓ after the 2D coordinate transformation and before the final Fourier-transforming lens. Another approach, which we implemented here, is to add at the output of the 1D spectral transformation a linear phase distribution along y extending from 0 to $2\pi\ell$, which is subsequently wrapped around the azimuthal direction after traversing the 2D coordinate transformation, thereby realizing OAM of order ℓ ⁵⁵.

For the sake of benchmarking, we also synthesized pulsed Bessel beams with separable spatio-temporal spectrum by circumventing the spectral analysis and 1D spectral transformation, and sending the input laser pulses directly to the 2D coordinate transformation. To match the temporal bandwidth of the pulsed Bessel beams to that of the 3D ST wave packets, we spectrally filter $\Delta\lambda = 0.3$ nm from the input spectrum via a planar Fabry-Pérot cavity.

Characterizing 3D ST wave packets

To verify the structure of the synthesized 3D ST wave packet, we characterize the field in four distinct domains: (1) the spatio-temporal spectrum to verify the square-root radial chirp (Fig. 4); (2) the time-averaged intensity to confirm diffraction-free propagation along z

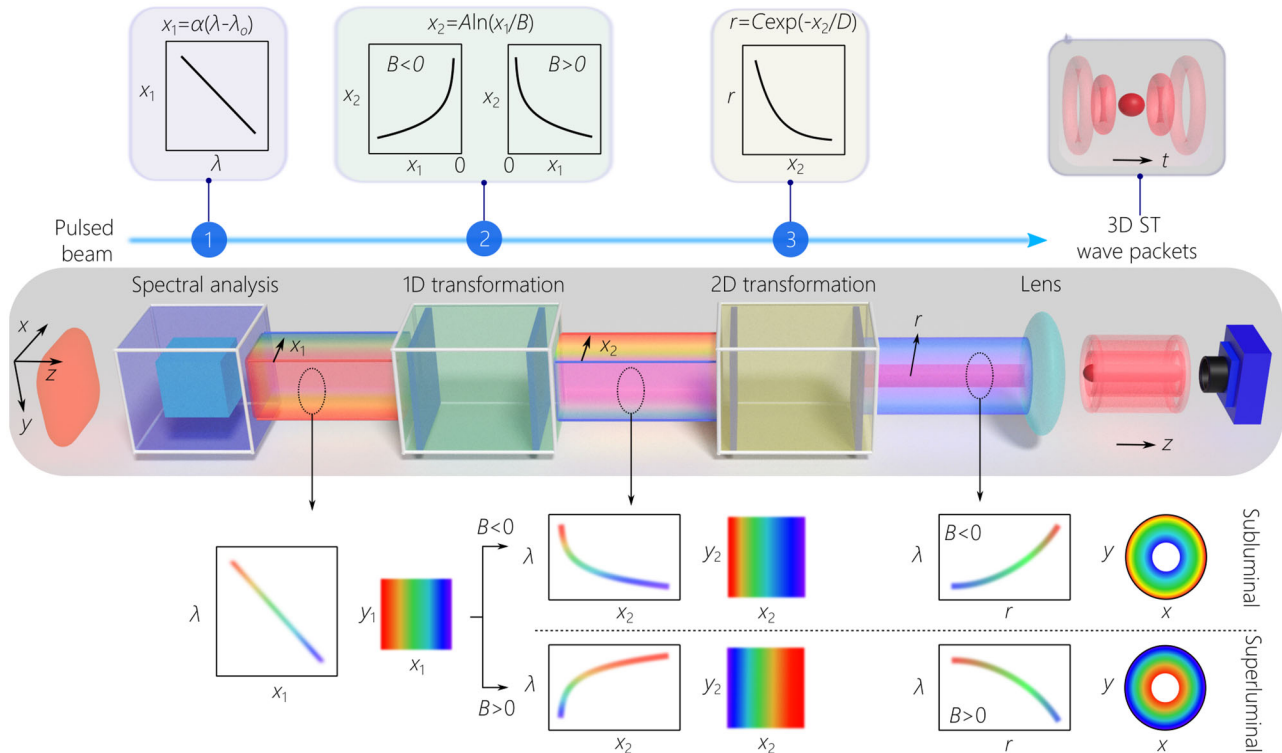


Fig. 3 | Schematic of the setup for synthesizing 3D ST wave packets. Starting with a plane-wave pulse on the left, spectral analysis resolves the spectrum in space and produces linear spatial chirp, $x_1(\lambda) = \alpha(\lambda - \lambda_0)$. The spectrally resolved field enters a tunable 1D spectral transformation formed of two spatial light modulators ‘reshuffles’ the wavelengths, $x_2(\lambda) = A \ln(\frac{x_1(\lambda)}{B})$. Opposite signs of chirp along x_2 are required for subluminal and superluminal wave packets. Next, a fixed 2D

coordinate transformation (implemented with two fixed phase plates) converts the vertical lines corresponding to different wavelengths into circles of radius $r(\lambda) = C \exp(-\frac{x_2(\lambda)}{D})$. Finally, a converging spherical lens produces the 3D ST wave packet. On the top, we plot the implemented spectral and spatial transformations; on the bottom, we illustrate the field structure at different points along the setup.

(Fig. 5); (3) time-resolved intensity measurements to reconstruct the wave-packet spatio-temporal profile and estimate the group velocity (Fig. 6); and (4) complex-field measurements to resolve the spiral phase of the ST-OAM wave packets (Fig. 7).

Spectral-domain characterization. We measure the spatio-temporal spectrum by scanning a single-mode fiber connected to an optical spectrum analyzer across the spectrally resolved field profile. We scan the fiber along x_1 after the spectral analysis stage and verify the linear spatial chirp (Supplementary Fig. 10), and then scan the fiber along x_2 after the 1D spectral transformation to confirm the implemented change in spatial chirp. The measurement is repeated for superluminal ($B = 10$ mm, $\tilde{v} \approx 1.37c$) and subluminal ($B = -10$ mm, $\tilde{v} \approx 0.83c$) wave packets, both with temporal bandwidth $\Delta\lambda \approx 0.3$ nm, pulse width of ~ 6 ps, and $\lambda_0 = 796.1$ nm. After the 2D coordinate transformation, the spectrum is arranged radially along an annulus rather than a rectilinear domain, as shown in Fig. 4a. By calibrating the conversion $x_2 \rightarrow r$ engendered by the 2D coordinate transformation, and combining with the measured spatial chirp $x_2(\lambda)$ at its input, we obtain the radial chirp $k_r(\lambda)$ as shown in Fig. 4b (Supplementary Fig. 15). We find at each radial position a narrow spectrum ($\delta\lambda \approx 50$ pm) whose central wavelength λ_c shifts quadratically with r , but with differently signed curvature for the superluminal and subluminal cases (Fig. 4c).

Propagation-invariance of the intensity distribution. The time-averaged intensity profile $I(x, y, z) \propto \int dt |E(x, y, z; t)|^2$ is captured by scanning a CCD camera along the propagation axis z after the Fourier transforming lens (Fig. 3). For each wave packet, we plot in Fig. 5 the intensity distribution (at a fixed axial plane $z = 30$ mm) in transverse and meridional planes. As a point of reference, we start with a pulsed

Bessel beam whose spatio-temporal spectrum is separable, where the spatial bandwidth is $\Delta k_r = 0.02$ rad/ μm and is centered at $k_r \approx 0.06$ rad/ μm (Fig. 5a). Here, the full temporal bandwidth $\Delta\lambda$ is associated with each spatial frequency k_r . The finite spatial bandwidth Δk_r renders the propagation distance finite⁵⁶, and we observe a Bessel beam comprising a main lobe of width $\Delta r \approx 30$ μm (FWHM) accompanied by several side lobes, which propagates for a distance $L_{\text{max}} \approx 50$ mm. For comparison, the Rayleigh range of a Gaussian beam with a similar size and central wavelength is $z_R \approx 1$ mm. By further increasing Δk_r to 0.07 rad/ μm while remaining centered at $k_r \approx 0.06$ rad/ μm as shown in Fig. 5b, the axial propagation distance is reduced proportionately to $L_{\text{max}} \approx 15$ mm, and the side lobes are diminished.

Now, rather than the separable spatio-temporal spectra for pulsed Bessel beams (Fig. 5a, b), we utilize the structured spatio-temporal spectra associated with 3D ST wave packets in which each k_r is associated with a single λ (Fig. 4), whose spatial bandwidths are all $\Delta k_r = 0.07$ rad/ μm centered at $k_r \approx 0.06$ rad/ μm , similarly to the pulsed Bessel beam in Fig. 5b. Despite the large spatial bandwidth, the one-to-one correspondence between k_r and λ curtails the effect of diffraction, leading to an increase in the propagation distance (Fig. 5c–e). The subluminal 3D ST wave packet ($\tilde{v} = 0.83c$) in Fig. 5c propagates for $L_{\text{max}} \approx 60$ mm, which is a $4 \times$ improvement compared with the separable Bessel beam and a $60 \times$ improvement compared with a Gaussian beam of the same spatial bandwidth. We observe a similar behavior for a superluminal 3D ST wave packet ($\tilde{v} = 1.37c$) in Fig. 5d, and a superluminal ST-OAM wave packet ($\tilde{v} = 1.16c$) with $\ell = 1$ in Fig. 5e.

Reconstructing the spatio-temporal profile and measuring the group velocity. The spatio-temporal intensity profile $I(x, y, z; t) = |E(x, y, z; t)|^2$ of the 3D ST wave packet is reconstructed by placing the

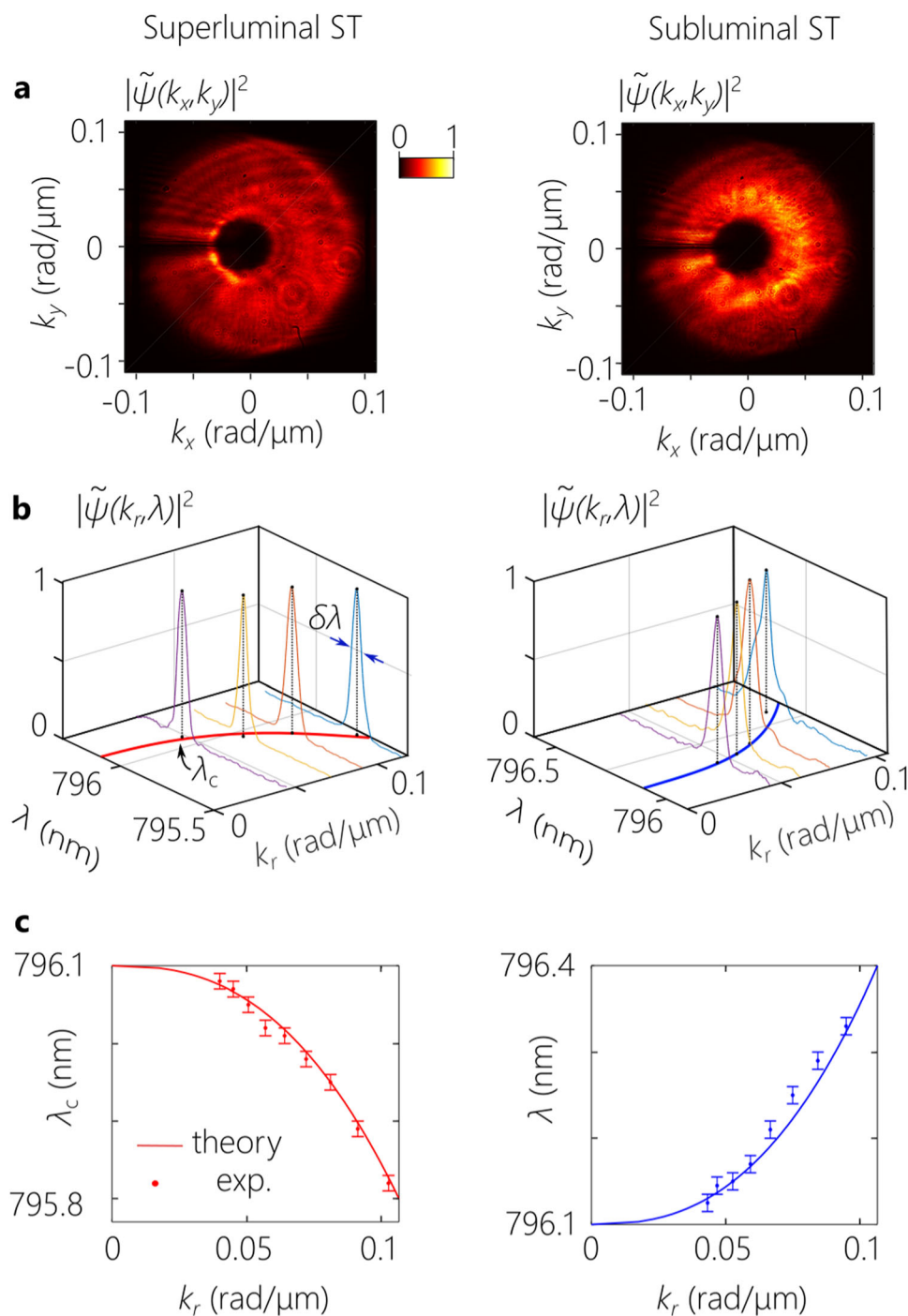


Fig. 4 | The spatio-temporal spectral structure of 3D ST wave packets. Measurements for a superluminal wave packet ($\tilde{v} \approx 1.37c$) are plotted in the left column, and those for its subluminal counterpart ($\tilde{v} \approx 0.83c$) are plotted in the column on the right. **a** Measured spatial spectrum $|\tilde{\psi}(k_x, k_y)|^2$ by a wavelength-insensitive camera showing an annular structure. **b** Measured temporal spectra at selected

radial positions revealing the radial chirp and the spectral uncertainty. **c** Measured radial chirp by plotting the central wavelength λ_c of the spectrum with radial spatial frequency k_r . Error bars in **c** represent the spectral resolution of the optical spectrum analyzer (OSA; Advantest AQ6317B) we made use to perform spectral measurements.

synthesizer (Fig. 3) in one arm of a Mach-Zehnder interferometer, while the initial 100-fs plane-wave pulses from the laser traverse an optical delay line τ in the reference arm (Fig. 6a). By scanning τ we reconstruct the spatio-temporal intensity profile in a meridional plane from the visibility of spatially-resolved interference fringes recorded by a CCD camera when the 3D ST wave packet and the reference pulse overlap in space and time. The reconstructed time-resolved intensity profile $I(0, y, z; t)$ of the 3D ST wave packets corresponding to those in Fig. 5c–e are plotted in Fig. 6b–d at multiple axial planes, which reveal

clearly the expected X-shaped profile that remains invariant over the propagation distance L_{\max} . In all cases, the on-axis pulse width, taken as the FWHM of $I(0, 0, 0; t)$, is $\Delta t \approx 6$ ps. The spatio-temporal intensity profile of the superluminal ST-OAM wave packet with $\ell=1$ in Fig. 6d reveals a similar X-shaped profile, but with a central null instead of a peak, as expected from the helical phase structure associated with the OAM mode.

A subtle distinction emerges between the subluminal and superluminal wave packets regarding the axial evolution of their spatio-

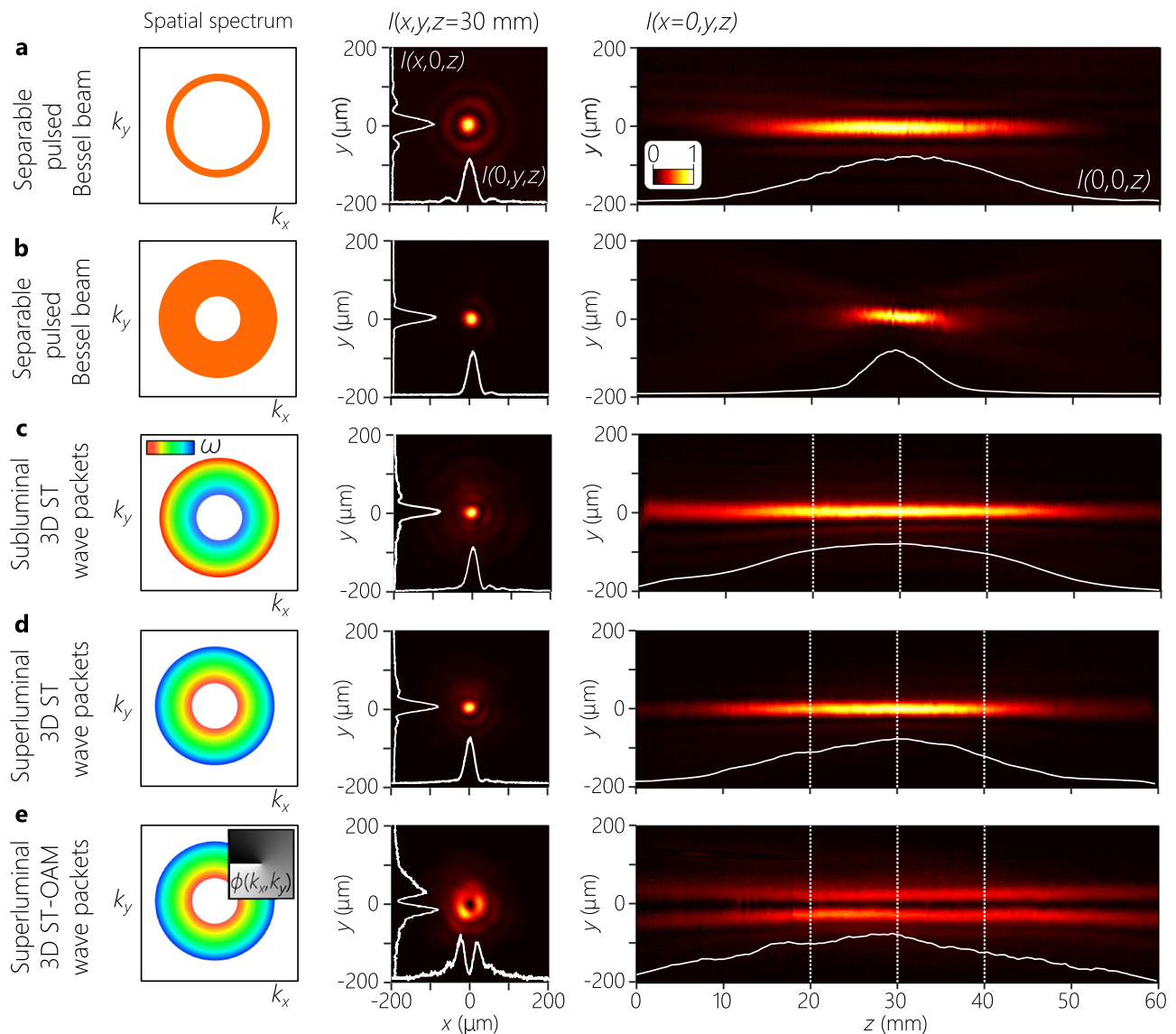


Fig. 5 | Measured transverse and axial time-averaged intensity for separable pulsed Bessel beams and 3D ST wave packets. In the first column, we illustrate the spatio-temporal structure; in the second, we plot the measured transverse intensity $I(x, y, z)$ at $z = 30$ mm, in addition to sections through $x = 0$ and $y = 0$ (white curves); and, in the third, we plot the measured intensity in a meridional plane $I(0, y, z)$. The white curve at the bottom of the panels in the last column is the on-axis intensity $I(0, 0, z)$, except in **e** where we use $y = 30$ μm . For all cases,

$\Delta\lambda = 0.3$ nm. **a** A separable pulsed Bessel beam with $\Delta k_r = 0.02$ rad/ μm . **b** A pulsed Bessel beam with $\Delta k_r = 0.07$ rad/ μm . **c–e** In all cases $\Delta k_r = 0.07$ rad/ μm as in **b**. **c** A subluminal ($\bar{v} = 0.83c$) 3D ST wave packet; **d** a superluminal ($\bar{v} = 1.37c$) 3D ST wave packet; and **e** a superluminal ($\bar{v} = 1.16c$) 3D ST-OAM wave packet with $\ell = 1$ (the inset in the first column is the associated transverse spectral phase distribution). The dotted vertical white lines in the third column in **c–e** identify the axial planes for the time-resolved measurements in Fig. 6.

temporal profile. It can be shown that in presence of finite spectral uncertainty $\delta\lambda$, the realized ST wave packet can be separated into the product of an ideal ST wave packet traveling indefinitely at \bar{v} and a long ‘pilot envelope’ traveling at c . The finite propagation distance L_{max} is then a consequence of temporal walk-off between the ST wave packet and the pilot envelope⁵². For subluminal ST wave packets, this results initially in a ‘clipping’ of the leading edge of the wave packet in (Fig. 6b at $z = 20$ mm), and ultimately a clipping of the trailing edge of the ST wave packet as the faster pilot envelope catches up with it (Fig. 6b at $z = 40$ mm). The opposite behavior occurs for the superluminal ST wave packet in Fig. 6c, d.

This experimental methodology also enables us to estimate the group velocity \bar{v} ^{28,30}. After displacing the CCD camera until the interference fringes are lost due to the mismatch between $\bar{v} = c \tan \theta$ for the ST wave packets and the reference pulses traveling at $\bar{v} = c$, we restore the interference by inserting a delay Δt (Fig. 6e), which allows us to

estimate \bar{v} for the 3D ST wave packet. By tuning B , we record a broad span of group velocities in the range from $\bar{v} \approx 0.7c$ to $\bar{v} \approx 1.8c$ in free space (Fig. 6f). The continuous tunability of the group velocity of 3D ST wave packets over the subluminal and superluminal ranges allows them to be exploited in applications previously proposed for ST light-sheets, such as for constructing in-line optical delay lines for all-optical communications²⁹, whereby the localization of 3D ST wave packets in both transverse dimensions can provide a significant advantage with regards to efficiently coupling into optical fibers.

Field amplitude and phase measurements. Lastly, we modify the measurement system in Fig. 6a by adding a small relative angle between the propagation directions of the 3D ST wave packets and the reference pulses, and make use of off-axis digital holography⁵⁷ to reconstruct the amplitude $|\psi(x, y, z; t)|$ and phase $\phi(x, y, z; t)$ of their complex field envelope $\psi(x, y, z; t) = |\psi(x, y, z; t)|e^{i\phi(x, y, z; t)}$ (Supplementary Note 3D). We

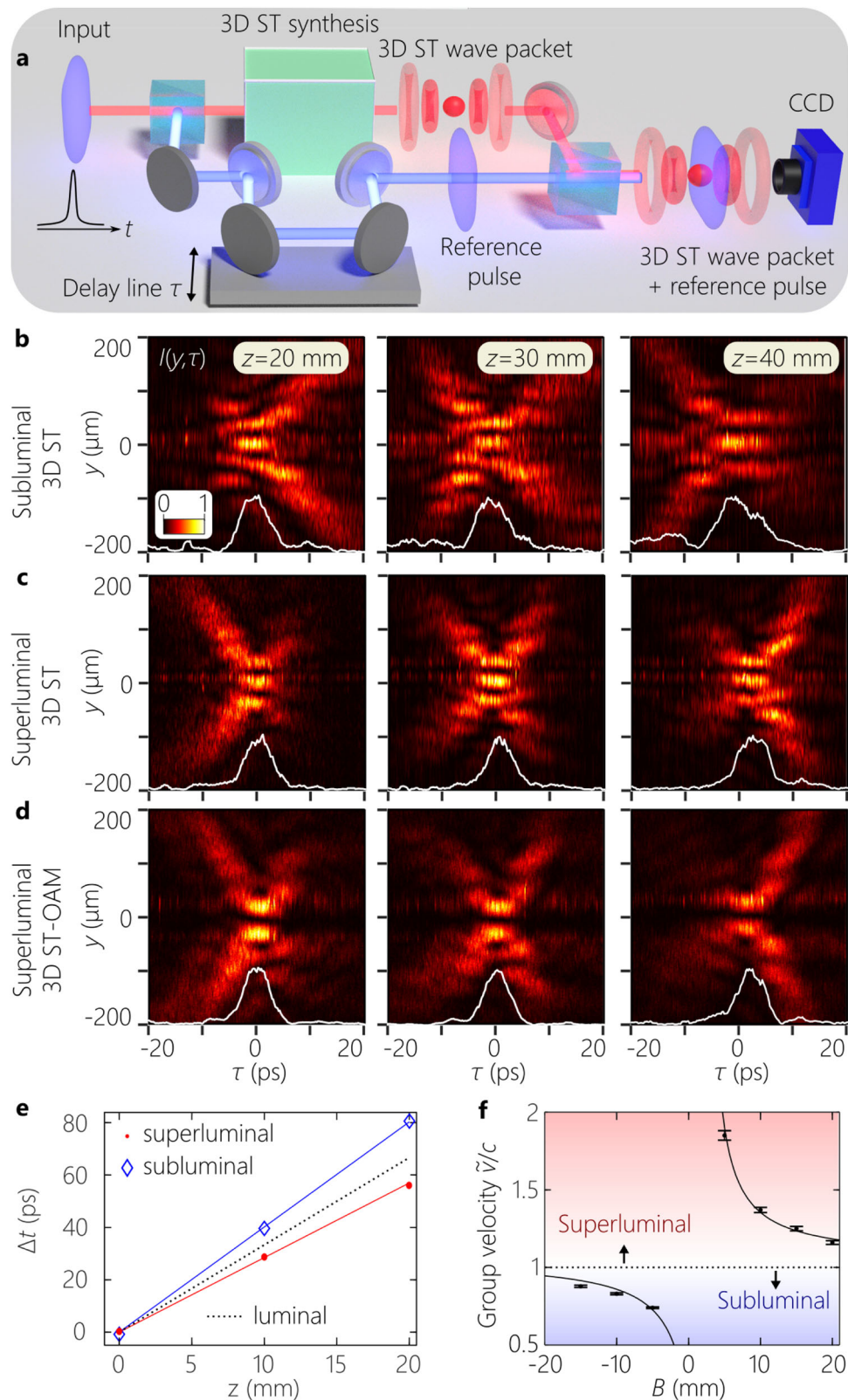


Fig. 6 | Reconstructing the spatio-temporal intensity profile and estimating the group velocity for 3D ST wave packets. **a** Schematic of the interferometric configuration for reconstructing $I(x, y, z; t)$ and estimating \tilde{v} . **b** Measured $I(0, y, z; \tau)$ at $z = 20, 30,$ and 40 mm for a subluminal ($\tilde{v} = 0.83c$) wave packet; **c** for a superluminal ($\tilde{v} = 1.37c$) wave packet; and **d** for a superluminal ($\tilde{v} = 1.16c$) wave packet endowed with the OAM mode $\ell = 1$. We also plot the section $y = 0$ through the intensity profile (white curve at the bottom of each panel), except in **d** where we

use $y = 30 \mu\text{m}$. **e** Measured group delay Δt at different axial planes for subluminal and superluminal 3D ST wave packets. The straight lines are theoretical expectations and the symbols are data points. **f** Plot of the estimated group velocity \tilde{v} with the 1D spectral transformation parameter B . The curve is the theoretical expectation $\tilde{v} = c/\tilde{n}$, with $\tilde{n} = 1 - \frac{2\ell^2}{B^2}$ (B in mm). Error bars correspond to the uncertainty in the measurement of \tilde{v} due to the finite pulse width of 3D ST wave packets; see Supplementary Note 3C.

reconstruct the complex field at a fixed axial plane $z = 30$ mm for the time delays: $\tau = -5, 0$, and 5 ps (Fig. 7). First, we plot the results for $|\psi(x, y, z; \tau)|$ and phase $\phi(x, y, z; \tau)$ for a superluminal 3D ST wave packet ($\tilde{v} = 1.1c$) with no OAM ($\ell = 0$). At the pulse center $\tau = 0$, the field is localized on the optical axis, whereas at $\tau = \pm 5$ ps the field spreads away from the center (Fig. 7a). For $\tau \neq 0$ we find a spherical transverse phase distribution that is almost flat at $\tau = 0$, similar to what one finds during the axial evolution of a Gaussian beam in space through its focal plane¹⁴.

After adding the OAM mode $\ell = 1$ to the field structure, a similar overall behavior is observed for the superluminal ST-OAM wave packet except for two significant features. First, a dip is observed on-axis in Fig. 7b, in lieu of the central peak in Fig. 7a, as a result of the phase singularity associated with the OAM mode. Second, the phase at the wave-packet center $\phi(x, y, z; 0)$ at $z = 30$ mm is almost flat, while a helical phase front corresponding to OAM of order $\ell = 1$ emerges as we move away from $\tau = 0$. Finally, we plot in Fig. 7c, d iso-amplitude surface contours ($0.6 \times$ and $0.15 \times$ the maximum amplitude I_{\max}) for the two 3D ST wave packets in Fig. 7a, b. We find a closed surface in Fig. 7c when $\ell = 0$, and a doughnut structure in Fig. 7d when $\ell = 1$ for the first contour $I = 0.6I_{\max}$ that captures the structure of the wave-packet center. The second contour for $I = 0.15I_{\max}$ captures the conic structure emanating from the wave-packet center that is responsible for the characteristic X-shaped spatio-temporal profile of all propagation-invariant wave packets in the paraxial regime.

Discussion

We have demonstrated a general procedure for spatio-temporal spectral modulation of pulsed optical fields that is capable of synthesizing 3D ST wave packets localized in all dimensions. At the heart of our experimental methodology lies the ability to sculpt the angular dispersion of a generic optical pulse in two transverse dimensions. Crucially, this approach produces the non-differentiable angular-dispersion necessary for propagation invariance²¹. Because such a capability has proven elusive to date, AD-free X-waves have been the sole class of 3D propagation-invariant wave packets conclusively produced in free space. Unfortunately, X-waves can exhibit only minuscule changes in the group velocity with respect to c (typically $\Delta\tilde{v} \sim 0.001c$) in the paraxial regime, and only superluminal group velocities are supported. Furthermore, ultrashort pulses of width < 20 fs are required to observe a clear X-shaped profile¹⁰, and OAM-carrying X-waves have not been realized to date. Even more stringent requirements are necessary for producing focus-wave modes, and consequently they have not been synthesized in three dimensions to date. By realizing instead propagation-invariant 3D ST wave packets, an unprecedented tunable span of group velocities has been realized, clear X-shaped profiles are observed with pulse widths in the picosecond regime, and they outperformed spectrally separable pulsed Bessel beams of the same spatial bandwidth with respect to their propagation distance and transverse side-lobe structure. In addition, we demonstrated propagation-invariant ST-OAM wave packets with tunable group velocity in free space.

Further optimization of the experimental layout is possible. We made use of four phase patterns to produce the target spatio-temporal spectral structure. It is conceivable that this spectral modulation scheme can be performed with only three phase patterns, or perhaps even fewer. Excitingly, a new theoretical proposal suggests that a single non-local nanophotonic structure can produce 3D ST wave packets through a process of spatio-temporal spectral filtering⁵⁸. This theoretical proposal indicates the role nanophotonics is poised to play in reducing the complexity of the synthesis system, potentially without recourse to filtering strategies.

Finally, efforts in the near future will be directed to reducing the spectral uncertainty $\delta\lambda$ and concomitantly approaching $\theta \rightarrow 45^\circ$ to increase the propagation length to the kilometer range²⁴. The

experimental procedure presented here can in principle be extended to the synthesis of other exotic variants of ST wave packet, such as abruptly focusing needle pulses⁵⁹ among other possibilities^{19,60}. With access to 3D ST wave packets, previous work on guided ST modes in planar wave-guides⁶¹ can be extended to conventional single-mode and multi-mode waveguides⁶², and potentially to optical fibers^{63–66}. Moreover, the localization in both transverse dimensions provided by 3D ST wave packets opens new avenues for nonlinear optics by increasing the intensity with respect to 2D ST wave packets, for introducing topological features such as spin texture in momentum space⁵⁸, and for the exploration of spatio-temporal vortices and polarization singularities⁶⁷. Our findings point therefore to profound new opportunities provided by the emerging field of space-time optics^{58,61,62,68–71}.

Methods

The 2D transformation used to construct the 3D STWP can be implemented by making use of *diffractive* optics^{53,55,72,73} or *refractive* optics⁵⁴. We exploited both types of phase plates in our experiments to imprint the desired phase profiles: diamond-edged refractive phase plates⁵⁴ and analog diffractive phase plates⁵⁵.

Refractive phase plates

The refractive optical elements used in our experiments are similar to those outlined by Lavery et al. in⁵⁴, in which the transformation parameters are $C = 4.77$ mm, $D = \frac{3.2}{\pi} \approx 1$ mm, and $d_2 = 310$ mm. Each phase plate is made of the polymer PMMA (Poly methyl methacrylate) with accurately manufactured height profiles $Z_1(x_3, y_3)$ and $Z_2(x_4, y_4)$ to imprint the required phase profiles. The phase encountered by light at a wavelength λ traversing a height Z of a material of refractive index n – with respect to the phase encountered over the same distance in vacuum – is given by $\Phi = 2\pi(n - 1)Z/\lambda$. Thus, the height profile of the first element is $Z_1(x_3, y_3) = \frac{\lambda}{2\pi(n-1)}\Phi_3(x_3, y_3)$ (Supplementary Fig. 14a) and that of the profile of the second element is $Z_2(x_4, y_4) = \frac{\lambda}{2\pi(n-1)}\Phi_4(x_4, y_4)$ (Supplementary Fig. 14b). Note that each surface height is wavelength-independent, and dispersion effects in the material manifest themselves as a change in the focal length d_2 of the integrated lens for different wavelengths. Hence, in the experiment the system can be tuned to a specific wavelength by changing the distance between the two elements.

The elements were diamond-machined using a Natotech, 3-axis (X,Z,C) ultra precision lathe (UPL) in combination with a Nanotech NFTS6000 fast tool servo (FTS) system. The machined PMMA surfaces had a radius of 5.64 mm, angular spacing 1° , radial spacing of 5 μm , a spindle speed of 500 RPM, a roughing feed rate 5 mm/minute with a cut depth of 20 μm , and a finishing feed rate of 1 mm/minute with a cut depth of 10 μm ⁷⁴. The total sag height difference for each part was relatively small (≈ 115 μm for surface 1 and ≈ 144 μm for surface 2). The transmission efficiency of the combination of the elements is $\approx 85\%$.

Diffractive phase plates. The diffractive phase plates were fabricated in fused silica using Clemson University facilities. The fabrication process is outlined in⁷⁵, which involves writing a binary phase grating on a stepper mask with an electron-beam and subsequently transferring this analog mask into a fused silica substrate with projection lithography. The phase grating period is designed to be larger than the cutoff period of the projection stepper for higher diffraction orders, so only the zeroth-order diffracted light from the stepper can be transmitted. The transmission coefficient of the stepper light is then a function of the duty cycle of the electron-beam-patterned binary phase grating. The spatial intensity distribution of light in the wafer plane can be controlled with a spatial duty cycle function, which then exposes the I-line resist with a spatially varying analog intensity profile. This allows fabrication of analog diffractive optics with a single exposure from the stepper rather than binary 2^n diffractive optics, resulting

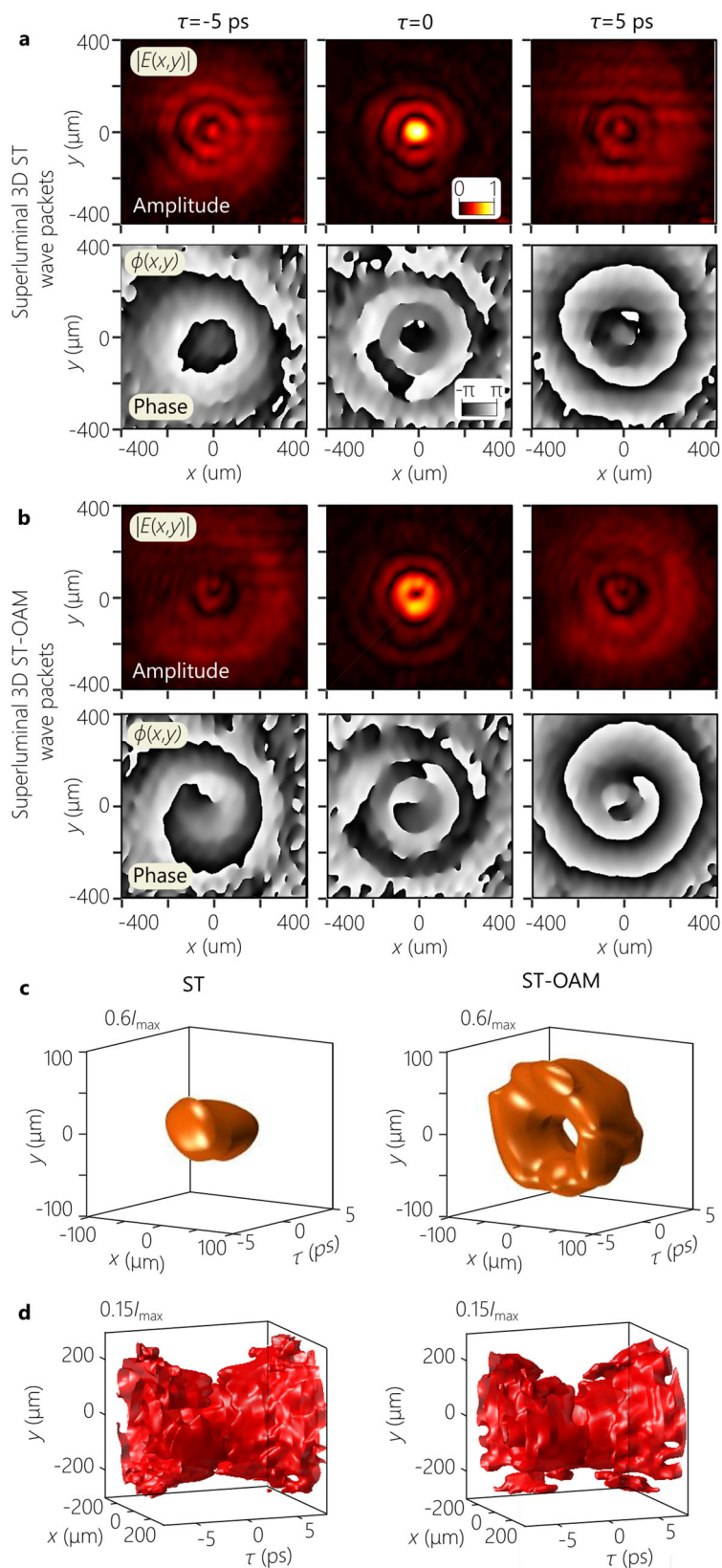


Fig. 7 | Measured complex-field amplitude and phase profiles for 3D ST wave packets with and without OAM. a Measured amplitude $|E(x,y)|$ (first row) and phase $\phi(x,y)$ (second row) at a fixed axial plane $z = 30$ mm (see Figs. 5 and 6) at delays $\tau = -5$ ps, $\tau = 0$ corresponding to the wave-packet center, and $\tau = 5$ ps for a

superluminal 3D ST wave packet with $\ell = 0$ and **a** $\ell = 1$. **c** Iso-amplitude contour $I = 0.6 I_{\text{max}}$ for the 3D ST wave packet from (a) and ST-OAM from (b). **d** Same as c but for the iso-amplitude contour $I = 0.15 I_{\text{max}}$.

in high-efficiency optics. The transmission efficiency of the combination of the two faces is $\approx 92\%$.

The design parameters for the analog diffractive phase plates are chosen as follows: $D = \frac{7}{\pi} \approx 2.2$ mm, $C = 6$ mm, $\lambda_0 = 798$ nm, and $d_2 = 225$ nm. These design parameters were optimized so the paraxial approximation remains valid over the desired transformation range of 5 mm.

Data availability

The data that support the plots within this paper and other findings of this study are available from the corresponding author upon reasonable request.

Code availability

The software code used for data acquisition and data analysis are available from the corresponding author upon reasonable request.

References

- Malomed, B. A., Mihalache, D., Wise, F. & Torner, L. Spatiotemporal optical solitons. *J. Opt. B* **7**, R53–R72 (2005).
- Saleh, M. B. E. A. & Teich, C. *Principles of Photonics* (Wiley, 2007)
- Chong, A., Renninger, W. H., Christodoulides, D. N. & Wise, F. W. Airy-Bessel wave packets as versatile linear light bullets. *Nat. Photon.* **4**, 103–106 (2010).
- Fülöp, J. A., & Hebling, J. *Applications of tilted-pulse-front excitation*, in Recent Optical and Photonic Technologies (ed. K. Y. Kim) (InTech, 2010).
- Torres, J. P., Hendrych, M. & Valencia, A. Angular dispersion: an enabling tool in nonlinear and quantum optics. *Adv. Opt. Photon.* **2**, 319–369 (2010).
- Donnelly, R. & Ziolkowski, R. W. Designing localized waves. *Proc. R. Soc. Lond. A* **440**, 541–565 (1993).
- Turunen, J. & Friberg, A. T. Propagation-invariant optical fields. *Prog. Opt.* **54**, 1–88 (2010).
- Brittingham, J. N. Focus wave modes in homogeneous Maxwell's equations: Transverse electric mode. *J. Appl. Phys.* **54**, 1179–1189 (1983).
- Saari, P. & Reivelt, K. Evidence of X-shaped propagation-invariant localized light waves. *Phys. Rev. Lett.* **79**, 4135–4138 (1997).
- Grunwald, R. et al. Generation and characterization of spatially and temporally localized few-cycle optical wave packets. *Phys. Rev. A* **67**, 063820 (2003).
- Kondakci, H. E. & Abouraddy, A. F. Diffraction-free pulsed optical beams via space-time correlations. *Opt. Express* **24**, 28659–28668 (2016).
- Parker, K. J. & Alonso, M. A. The longitudinal iso-phase condition and needle pulses. *Opt. Express* **24**, 28669–28677 (2016).
- Wong, L. J. & Kaminer, I. Ultrashort tilted-pulse-front pulses and nonparaxial tilted-phase-front beams. *ACS Photon.* **4**, 2257–2264 (2017).
- Porras, M. A. Gaussian beams diffracting in time. *Opt. Lett.* **42**, 4679–4682 (2017).
- Efremidis, N. K. Spatiotemporal diffraction-free pulsed beams in free-space of the Airy and Bessel type. *Opt. Lett.* **42**, 5038–5041 (2017).
- Kondakci, H. E. & Abouraddy, A. F. Diffraction-free space-time beams. *Nat. Photon.* **11**, 733–740 (2017).
- Yessenov, M., Bhaduri, B., Kondakci, H. E. & Abouraddy, A. F. Classification of propagation-invariant space-time light-sheets in free space: Theory and experiments. *Phys. Rev. A* **99**, 023856 (2019).
- Yessenov, M., Bhaduri, B., Kondakci, H. E. & Abouraddy, A. F. Weaving the rainbow: Space-time optical wave packets. *Opt. Photon. N.* **30**, 34–41 (2019).
- Wong, L. J. Propagation-invariant space-time caustics of light. *Opt. Express* **29**, 30682 (2021).
- Hall, L. A. & Abouraddy, A. F. Consequences of non-differentiable angular dispersion in optics: tilted pulse fronts versus space-time wave packets. *Opt. Express* **30**, 4817–4832 (2022).
- Yessenov, M., Hall, L. A. & Abouraddy, A. F. Engineering the optical vacuum: Arbitrary magnitude, sign, and order of dispersion in free space using space-time wave packets. *ACS Photon.* **8**, 2274–2284 (2021).
- Hall, L. A., Yessenov, M. & Abouraddy, A. F. Space-time wave packets violate the universal relationship between angular dispersion and pulse-front tilt. *Opt. Lett.* **46**, 1672–1675 (2021).
- Hall, L. A., & Abouraddy, A. F. A universal angular-dispersion synthesizer. *arXiv:2109.13987* (2021).
- Bhaduri, B. et al. Broadband space-time wave packets propagating 70 m. *Opt. Lett.* **44**, 2073–2076 (2019).
- Salo, J. & Salomaa, M. M. Diffraction-free pulses at arbitrary speeds. *J. Opt. A* **3**, 366–373 (2001).
- Valtna, H., Reivelt, K. & Saari, P. Methods for generating wideband localized waves of superluminal group velocity. *Opt. Commun.* **278**, 1–7 (2007).
- Zamboni-Rached, M. & Recami, E. Subluminal wave bullets: Exact localized subluminal solutions to the wave equations. *Phys. Rev. A* **77**, 033824 (2008).
- Kondakci, H. E. & Abouraddy, A. F. Optical space-time wave packets of arbitrary group velocity in free space. *Nat. Commun.* **10**, 929 (2019).
- Yessenov, M., Bhaduri, B., Delfyett, P. J. & Abouraddy, A. F. Free-space optical delay line using space-time wave packets. *Nat. Commun.* **11**, 5782 (2020).
- Bhaduri, B., Yessenov, M. & Abouraddy, A. F. Anomalous refraction of optical spacetime wave packets. *Nat. Photon.* **14**, 416–421 (2020).
- Hall, L. A., Yessenov, M., Ponomarenko, S. A. & Abouraddy, A. F. The space-time Talbot effect. *APL Photon.* **6**, 056105 (2021).
- Vaughan, J. C., Feurer, T. & Nelson, K. A. Automated spatiotemporal diffraction of ultrashort laser pulses. *Opt. Lett.* **28**, 2408–2410 (2003).
- Jhajj, N. et al. Spatiotemporal optical vortices. *Phys. Rev. X* **6**, 031037 (2016).
- Hancock, S. W., Zahedpour, S., Goffin, A. & Milchberg, H. M. Free-space propagation of spatiotemporal optical vortices. *Optica* **6**, 1547–1553 (2019).
- Chong, A., Wan, C., Chen, J. & Zhan, Q. Generation of spatiotemporal optical vortices with controllable transverse orbital angular momentum. *Nat. Photon.* **14**, 350–354 (2020).
- Cao, Q. et al. Sculpturing spatiotemporal wavepackets with chirped pulses. *Photon. Res.* **9**, 2261–2264 (2021).
- Wan, C., Cao, Q., Chen, J., Chong, A., & Zhan, Q. Photonic toroidal vortex. *arXiv:2109.02833* (2021).
- Hancock, S. W., Zahedpour, S. & Milchberg, H. M. Second-harmonic generation of spatiotemporal optical vortices and conservation of orbital angular momentum. *Optica* **8**, 594–597 (2021).
- Hancock, S. W., Zahedpour, S. & Milchberg, H. M. Mode structure and orbital angular momentum of spatiotemporal optical vortex pulses. *Phys. Rev. Lett.* **127**, 193901 (2021).
- Bryngdahl, O. Geometrical transformations in optics. *J. Opt. Soc. Am. A* **64**, 1092–1099 (1974).
- Hossack, W. J., Darling, A. M. & Dahdouh, A. Coordinate transformations with multiple computer-generated optical elements. *J. Mod. Opt.* **34**, 1235–1250 (1987).
- Allen, L., Beijersbergen, M. W., Spreeuw, R. J. C. & Woerdman, J. P. Orbital angular momentum of light and the transformation of Laguerre-Gaussian laser modes. *Phys. Rev. A* **45**, 8185–8189 (1992).
- Ornigotti, M., Conti, C. & Szameit, A. Effect of orbital angular momentum on nondiffracting ultrashort optical pulses. *Phys. Rev. Lett.* **115**, 100401 (2015).

44. Porras, M. A. & García-Álvarez, Raúl Broadband x waves with orbital angular momentum. *Phys. Rev. A* **105**, 013509 (2022).
45. Porras, M. A. Upper bound to the orbital angular momentum carried by an ultrashort pulse. *Phys. Rev. Lett.* **122**, 123904 (2019).
46. Porras, M. A. & Conti, C. Couplings between the temporal and orbital angular momentum degrees of freedom in ultrafast optical vortices. *Phys. Rev. A* **101**, 063803 (2020).
47. Bélanger, P. A. Lorentz transformation of packetlike solutions of the homogeneous-wave equation. *J. Opt. Soc. Am. A* **3**, 541–542 (1986).
48. Saari, P. & Reivelt, K. Generation and classification of localized waves by Lorentz transformations in Fourier space. *Phys. Rev. E* **69**, 036612 (2004).
49. Longhi, S. Gaussian pulsed beams with arbitrary speed. *Opt. Express* **12**, 935–940 (2004).
50. Kondakci, H. E. & Abouraddy, A. F. Airy wavepackets accelerating in space-time. *Phys. Rev. Lett.* **120**, 163901 (2018).
51. Glebov, L. B. et al. Volume-chirped Bragg gratings: monolithic components for stretching and compression of ultrashort laser pulses. *Opt. Eng.* **53**, 051514 (2014).
52. Yessenov, M. et al. What is the maximum differential group delay achievable by a space-time wave packet in free space? *Opt. Express* **27**, 12443–12457 (2019).
53. Berkhout, G. C. G., Lavery, M. P. J., Courtial, J., Beijersbergen, M. W. & Padgett, M. J. Efficient sorting of orbital angular momentum states of light. *Phys. Rev. Lett.* **105**, 153601 (2010).
54. Lavery, M. P. J. et al. Refractive elements for the measurement of the orbital angular momentum of a single photon. *Opt. Express* **20**, 2110–2115 (2012).
55. Li, W. & Johnson, E. G. Rapidly tunable orbital angular momentum (OAM) system for higher order Bessel beams integrated in time (HOBBIT). *Opt. Express* **27**, 3920–3934 (2019).
56. Durnin, J., Miceli, J. J. & Eberly, J. H. Diffraction-free beams. *Phys. Rev. Lett.* **58**, 1499–1501 (1987).
57. Sánchez-Ortiga, E., Doblaz, A., Saavedra, G., Martínez-Corral, M. & García-Sucerquia, J. Off-axis digital holographic microscopy: practical design parameters for operating at diffraction limit. *Appl. Opt.* **53**, 2058–2066 (2014).
58. Guo, C., Xiao, M., Orenstein, M. & Fan, S. Structured 3D linear space-time light bullets by nonlocal nanophotonics. *Light.: Sci. Appl.* **10**, 1–15 (2021).
59. Wong, L. J. & Kaminer, I. Abruptly focusing and defocusing needles of light and closed-form electromagnetic wavepackets. *ACS Photon.* **4**, 1131–1137 (2017).
60. Wong, L. J., Christodoulides, D. N. & Kaminer, I. The complex charge paradigm: A new approach for designing electromagnetic wavepackets. *Adv. Sci.* **7**, 1903377 (2020).
61. Shiri, A., Yessenov, M., Webster, S., Schepler, K. L. & Abouraddy, A. F. Hybrid guided space-time optical modes in unpatterned films. *Nat. Commun.* **11**, 6273 (2020).
62. Guo, C. & Fan, S. Generation of guided space-time wave packets using multilevel indirect photonic transitions in integrated photonics. *Phys. Rev. Res.* **3**, 033161 (2021).
63. Ruano, P. N., Robson, C. W. & Ornigotti, M. Localized waves carrying orbital angular momentum in optical fibers. *J. Opt.* **23**, 075603 (2021).
64. Béjot, P. & Kibler, B. Spatiotemporal helicon wavepackets. *ACS Photon.* **8**, 2345–2354 (2021).
65. Kibler, B. & Béjot, P. Discretized conical waves in multimode optical fibers. *Phys. Rev. Lett.* **126**, 023902 (2021).
66. P., BéjotB., Kibler, Quadrics for structuring space-time wavepackets, arXiv:2202.00407 (2022).
67. Bliokh, K. Y. & Nori, F. Spatiotemporal vortex beams and angular momentum. *Phys. Rev. A* **86**, 033824 (2012).
68. Sainte-Marie, A., Gobert, O. & Quéré, F. Controlling the velocity of ultrashort light pulses in vacuum through spatio-temporal couplings. *Optica* **4**, 1298–1304 (2017).
69. Froula, D. H. et al. Spatiotemporal control of laser intensity. *Nat. Photon.* **12**, 262–265 (2018).
70. Shaltout, A. M. Spatiotemporal light control with frequency-gradient metasurfaces. *Science* **365**, 374–377 (2019).
71. Zdagkas, A., Shen, Y., Papisimakis, N., & Zheludev, N.I. Observation of toroidal pulses of light, arXiv:2102.03636 (2021)
72. Lavery, M. P. J., Berkhout, G. C. G., Courtial, J. & Padgett, M. J. Measurement of the light orbital angular momentum spectrum using an optical geometric transformation. *J. Opt.* **13**, 064006 (2011).
73. Berkhout, G. C. G., Lavery, M. P. J., Padgett, M. J. & Beijersbergen, M. W. Measuring orbital angular momentum superpositions of light by mode transformation. *Opt. Lett.* **36**, 1863–1865 (2011).
74. Dow, T. A., Miller, M. H. & Falter, P. J. Application of a fast tool servo for diamond turning of non-rotationally symmetric surfaces. *Precis. Eng.* **13**, 243–250 (1991).
75. Sung, J. W., Hockel, H., Brown, J. D. & Johnson, E. G. Development of a two-dimensional phase-grating mask for fabrication of an analog-resist profile. *Appl. Opt.* **45**, 33–43 (2006).

Acknowledgements

We thank OptiGrate Company for making volume Bragg gratings, and Dr. Peter J. Delfyett and Dr. Ivan Divliansky for lending equipment. We thank L. A. Hall, A. Shiri, K. L. Schepler, L. Mach, M. G. Vazimali, I. Hatipoglu, and M. Eshaghi for useful discussions. M.Y. and A.F.A. were supported by the U.S. Office of Naval Research (ONR) under contracts N00014-17-1-2458, N00014-19-1-2192, and N00014-20-1-2789. J.F. and E.G.J. were supported by ONR contract N00014-20-1-2558. M.A.A. was funded by the Excellence Initiative of Aix Marseille University – A*MIDEX, a French ‘Investissements d’Avenir’ programme.

Author contributions

A.F.A. and M.Y. developed the concept. M.Y. designed the experiments, carried out the measurements, and analyzed the data. Z.C. and M.P.J.L. designed and manufactured the diamond-machined refractive elements for the 2D coordinate transformation. J.F. and E.G.J. designed and fabricated the analog diffractive phase plates for the 2D coordinate transformation. M.A.A. and A.F.A. developed the theoretical aspects. A.F.A. supervised the research. All the authors contributed to writing the paper.

Competing interests

The authors declare no competing interests.

Additional information

Supplementary information The online version contains supplementary material available at <https://doi.org/10.1038/s41467-022-32240-0>.

Correspondence and requests for materials should be addressed to Murat Yessenov or Ayman F. Abouraddy.

Peer review information *Nature Communications* thanks Liang Jie Wong and the other, anonymous, reviewer(s) for their contribution to the peer review of this work.

Reprints and permission information is available at <http://www.nature.com/reprints>

Publisher’s note Springer Nature remains neutral with regard to jurisdictional claims in published maps and institutional affiliations.

Open Access This article is licensed under a Creative Commons Attribution 4.0 International License, which permits use, sharing, adaptation, distribution and reproduction in any medium or format, as long as you give appropriate credit to the original author(s) and the source, provide a link to the Creative Commons license, and indicate if changes were made. The images or other third party material in this article are included in the article's Creative Commons license, unless indicated otherwise in a credit line to the material. If material is not included in the article's Creative Commons license and your intended use is not permitted by statutory regulation or exceeds the permitted use, you will need to obtain permission directly from the copyright holder. To view a copy of this license, visit <http://creativecommons.org/licenses/by/4.0/>.

© The Author(s) 2022